Materials Horizons

ROYAL SOCIETY OF CHEMISTRY

COMMUNICATION

View Article Online
View Journal | View Issue

Cite this: *Mater. Horiz.*, 2024, 11, 5295

Received 28th May 2024,
Accepted 26th July 2024

DOI: 10.1039/d4mh00667d

rsc.li/materials-horizons

Ferroelectric, flexoelectric and photothermal coupling in PVDF-based composites for flexible photoelectric sensors†

Lu Wang,[ab] Muzaffar Ahmad Boda,[a] Chen Chen,[a] Xiang He[a] and Zhiguo Yi *[ab]

A ferroelectric polyvinylidene fluoride (PVDF) film with excellent flexibility possesses great potential for photodetection and wearable devices. However, the relatively weak photo-absorption and the consequent small photocurrent limit its photofunctional properties. Herein, we embedded a strongly visible-light active material system, $0.5Ba(Zr_{0.08}Ti_{0.8}Mn_{0.12})O_3$–$0.5(Ba_{0.7}Ca_{0.3})TiO_3$ (BZTM–BCT) loaded with Ag and Au nanoparticles, into a PVDF film, which demonstrates a significantly higher photovoltaic response in the whole visible light range with a β-phase content of over 90%. In a state of "bending + poling", the PVDF/BZTM–BCT:Au film presents an optimal response for photoelectric properties by exhibiting a photocurrent that is 57 times higher than that of a pure PVDF film when illuminated with 405 nm LED light at 100 mW cm^{-2}. Photoexcitation and thermal excitation jointly contribute to the generation of free carriers, while the flexoelectric and ferroelectric coupling electric field provides a greater driving force for carrier separation and transport. More interestingly, composite film-based photoelectric sensors can simultaneously respond to light and the movement and deformation of contacted things, indicating its potential in versatile applications. Overall, this work puts forward a new route for designing new flexible multifunctional photoelectric devices.

New concepts

Most conventional ferroelectric photovoltaic devices are based on inorganic ferroelectric ceramics, limiting its applications in flexible fields. Starting from photoexcited carrier generation and transport, we proposed a ferroelectric, flexoelectric and photothermal coupling strategy to achieve excellent photovoltaic output in a flexible composite film, which can sense not only light, but also the deformation and movement of its contacted things. This concept was confirmed through embedding Au or Ag nanoparticle-loaded $0.5Ba(Zr_{0.08}Ti_{0.8}Mn_{0.12})O_3$–$0.5(Ba_{0.7}Ca_{0.3})TiO_3$ ferroelectric particles into the PVDF film. Under light illumination, free carriers comprise photocarriers excited by partial photons and thermal carriers injected from metal nanoparticles into ceramic particles. Concurrently, when poling and bending the film, the ferroelectric and flexoelectric fields provide a driving force for carrier transport. The simultaneous regulations of photogenerated carrier generation and transport improve the photovoltaic current of the PVDF film by one order of magnitude. It provides a new route to explore flexible versatile photodetectors.

Introduction

Flexible optoelectronic sensors present substantial prospects in diverse fields, such as wearable devices, environmental monitoring and human-machine interconnection.[1–4] In this context, ferroelectric materials with excellent spontaneous polarization are promising candidates as they provide the necessary driving force for the separation of photogenerated electron–hole pairs.[5–7] Particularly, polyvinylidene fluoride (PVDF), as an excellent flexible ferroelectric material, has attracted widespread attention in recent years, especially in detecting near-infrared irradiation *via* the light induced pyroelectric effect.[8–11] However, pyroelectric photodetectors cannot be applied to constant light and often require an additional rectifying circuit in practical applications. By contrast, sensors based on the photovoltaic effect are more prevalent. Unfortunately, in its pure composition, PVDF exhibits weak ferroelectricity, triggering an almost negligible photovoltaic response. Although ferroelectric polarization can be enhanced by embedding fillers into PVDF films,[12,13] few research studies have focused on achieving this enhancement to improve their photovoltaic properties for application in photoelectric sensors.

The flexoelectric effect, known as strain gradient-induced electric polarization,[14] is not restricted by crystalline symmetry and temperature.[5,15,16] Thus, it can be applied in all dielectrics, including ferroelectrics and non-ferroelectrics. They can generate an uneven strain when bending,[17,18] polishing[19] or designing

[a] *State Key Laboratory of High Performance Ceramics and Superfine Microstructure, Shanghai Institute of Ceramics, Chinese Academy of Sciences, Shanghai 200050, China. E-mail: zhiguo@mail.sic.ac.cn*

[b] *Center of Materials Science and Optoelectronics Engineering, University of Chinese Academy of Science, Beijing, 100049, China*

† Electronic supplementary information (ESI) available. See DOI: https://doi.org/10.1039/d4mh00667d

the materials in an irregular shape.[20] This has been explored to induce an obvious photovoltaic response in unidirectionally polished $BiVO_4$ ceramics,[19] tip-contacted $SrTiO_3$ ceramics[21] and oscillating $MAPbI_3$ crystals.[22] An additional control can be achieved by combining the strain gradient with electric poling, under which electric polarization in the same directions can be superimposed and neutralized in opposite directions.[23] These findings provide a tremendous possibility for designing photovoltaic devices with excellent photoelectric properties. Because the strain gradient is linearly dependent on the sample size,[24,25] the films present great superiority over bulk samples. This is not only due to the smaller thickness, but also the excellent flexibility, making the films bend more easily. Hence, the flexo-photovoltaic response in PVDF-based films shows promise in producing efficient flexible photo-detectors.

Apart from the dynamics of photogenerated carriers, the photovoltaic response is also determined by the carrier concentration, which is more dependent on temperature than light intensity when the temperature exceeds a certain point. Among previous research studies, plasmonic metal nanoparticles (NPs) like Au and Ag NPs are often loaded on the ferroelectric semiconductors to improve their photocatalytic properties or photoelectric output through the local surface plasmonic resonance (LSPR) effect,[26–29] by which the hot carriers in metal NPs cross the metal NPs/ferroelectrics Schottky junction into the ferroelectrics. Theoretically, a temperature increase that occurs through a photothermal effect triggered by light–matter interaction will also promote the generation of hot carriers, and thus improve the photoelectric response. In this study, a compositionally engineered ferroelectric material system $0.5Ba(Zr_{0.08}Ti_{0.8}Mn_{0.12})O_3$–$0.5(Ba_{0.7}Ca_{0.3})TiO_3$ (BZTM–BCT) particles loaded with Ag and Au nanoparticles is embedded into PVDF to obtain a significant photovoltaic response in the illumination of all visible light wavelengths. The coupling of ferroelectric, flexoelectric and photothermal effects makes the film show a significantly higher photocurrent. The PVDF/BZTM–BCT:Au film achieves an improvement by about 57 times under 405 nm light at 100 mW cm^{-2}. The hot carrier injection from Au NPs into BZTM–BCT contributes 73% of the photocurrents. Interestingly, the photoelectric sensor responds not only to light, but also to the movement of contacted things due to the photocurrent dependence on bending, indicating its multifunctional applications.

Results and discussion

Structure and physical characterization

The structural and physical characterizations of the Au and Ag-loaded BZTM–BCT particles are summarized in Fig. 1. The preparation process of the BZTM–BCT:Au/Ag particles made through facile solution methods is briefly described in Fig. 1a. The detailed procedures are provided in the Experimental section (ESI†). In the XRD spectra shown in Fig. 1b, the peaks for all of these samples are well indexed to the tetragonal perovskite phase, consistent with the BZT–BCT particles. Peaks in the Mn-doped BZT–BCT shift towards the higher angle (Fig. S1, ESI†), indicating that the Mn element induces a lattice contraction in BZT–BCT. Peaks identified at 38° correspond to the (111) crystal plane of the cubic phase of Au and Ag NPs, which confirms that both are successfully loaded over BZTM–BCT.

The UV-vis light absorption spectra of the BZT–BCT based samples are given in Fig. 1c. Pure BZT–BCT particles show absorption to near-UV light only. However, after doping with Mn, the absorption range is extended to the whole visible light zone, indicating that Mn acts as a donor dopant that substantially reduces the bandgap of BZT–BCT.[30] Further extension in the absorption edge is observed when the resulting BZTM–BCT sample is loaded with Au and Ag NPs, which is due to the LSPR effect. The XPS measurements confirm that the increasing absorption is mainly attributed to the metallic Au and Ag, but not their oxides. As shown in Fig. 1d, the survey scan spectra display all of the peaks corresponding to all of the elements existing in the BZTM–BCT composition, and the peaks ascribed to Au 4f and Ag 3d occur in the BZTM–BCT:Au and BZTM–BCT:Ag samples, respectively. High-resolution Au 4f and Ag 3d XPS tests were carried out to analyze their chemical states. The peaks located at 83.7 eV and 87.4 eV are caused by Au $4f_{7/2}$ and Au $4f_{5/2}$, respectively (Fig. 1e). The two additional doublets are mainly attributed to the Ba 3d orbital, which indicates that Ba has at least two chemical states.[28,31] This phenomenon is reasonable because Ti, Mn, and Zr do coexist in the B-site of the ABO_3 structure. The peaks appearing at 368.0 eV and 374.0 eV are attributed to Ag $3d_{5/2}$ and Ag $3d_{3/2}$, respectively (Fig. 1f).[32] These results confirm that metallic Au and Ag are successfully deposited on the BZTM–BCT particles and not their oxides.

The morphology and lattice profiles of BZTM–BCT with Au and Ag nanoparticles are observed through TEM. Fig. 1g and h demonstrate the successful crystallization and distribution of Au and Ag NPs on the BZTM–BCT particles. The grain sizes of the BZTM–BCT are hundreds of nanometers, while the sizes of the Au and Ag NPs are in tens of nanometers (Fig. 1g1 and h1). The lattice fringes are clearly observed from the HRTEM images. Interplanar spacings of 2.38 Å and 2.89 Å, shown in Fig. 1g2, are in agreement with the (111) and (110) planes of tetragonal BZT–BCT, respectively. The interplanar distances of the Au and Ag NPs presented in Fig. 1g4 and h2 are both about 2.32 Å, corresponding to the (111) planes of cubic Au and Ag NPs. An excellent contact interface between the metal NPs and BZTM–BCT particles is also observed, which is beneficial to the formation of the Schottky junction and carrier transport. The lattice fringes were further analyzed by the SAED patterns (Fig. 1g3 and the insert image in Fig. 1h). Diffraction spots of the Au and Ag NPs are thoroughly mixed with that of BZTM–BCT, but are still clearly distinguished. These results are consistent with the XRD analysis, and therefore further validate that the Au and Ag NPs with great crystallinity are successfully deposited on the BZTM–BCT particles.

Fig. 2 presents the structure and physical properties of the as-prepared PVDF composite films. Fig. 2a schematically depicts the sandwich-like flexible PVDF composite films that we designed, in which ceramic particles with different compositions are uniformly embedded into the PVDF films (Fig. 2b and Fig. S2, ESI†), with almost no cracks or holes. These results confirm the formation of the good-quality PVDF composite films. The thicknesses of all of the films are about 10 μm (Fig. S3, ESI†). XRD measurements were carried out to identify

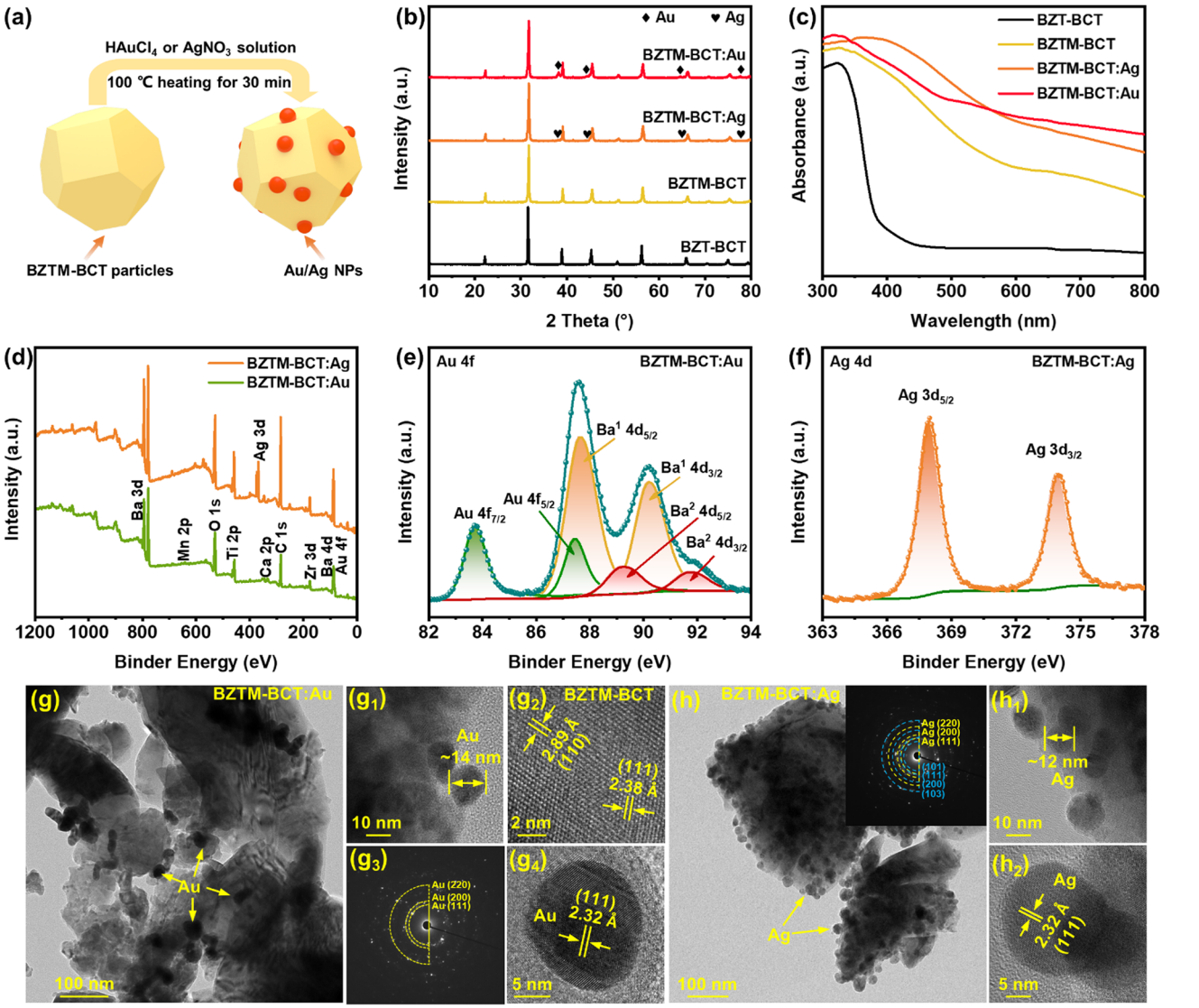

Fig. 1 Structural and physical properties of the Au and Ag-loaded BZTM–BCT particles. (a) Schematic preparation processes for the BZTM–BCT:Au/Ag heterostructures. (b) XRD spectra and (c) UV-vis spectra for different ceramic particles. XPS spectra for BZTM–BCT:Au/Ag particles: survey scan (d), Au 4f for BZTM–BCT:Au (e) and Ag 4d for BZTM–BCT:Ag (f). TEM, HRTEM and SAED images for BZTM–BCT:Au (g) and BZTM–BCT:Ag (h).

the phase structures and components of the composite films (Fig. 2c). The peaks at 18.3° and 20.2°, corresponding to the (020) and (110) planes, respectively, are indicators of the non-polar α phase and polar β phase of the pure PVDF film.[33,34] Peaks corresponding to base ceramic particles are clearly visible, but the peaks corresponding to Au and Ag NPs are difficult to identify as their relative content is very low. The phase components of these composite films were further analyzed through FTIR measurements. As shown in Fig. 2d, the α and β phases are characterized by the peaks at 771 and 835 cm^{-1}, respectively.[35] The introduction of ferroelectric ceramic particles is helpful to increase the β phase fraction $F(\beta)$ of the PVDF film.[13,18] $F(\beta)$ can be calculated through eqn (1):[11]

$$F(\beta) = \frac{A_\beta}{1.26A_\alpha + A_\beta} \quad (1)$$

where A_α and A_β are the areas of the peaks at 771 and 835 cm^{-1}, respectively. The $F(\beta)$ of the pure PVDF is about 82% (Fig. S4, ESI†). It reaches about 90% after introducing ceramic particles, and further increases to about 93% after depositing the Au and Ag NPs on the BZTM–BCT particles. The higher $F(\beta)$ may be caused by the stronger ferroelectricity of the conductive nanomaterials/ferroelectric composites, which has been widely reported.[29,36,37]

The photographs of five PVDF composite films with different ceramic particles are given in Fig. 2e. It can be seen that the pure PVDF film is almost transparent, while its transparency is greatly reduced after introducing ceramic particles. The PVDF film with BZT–BCT particles becomes white and the PVDF films with different BZTM–BCT particles become brown, but with slightly varying brightness. After depositing the Au and Ag NPs, the stronger absorptions of the films cause their color to become darker. Additionally, the films can be greatly bent,

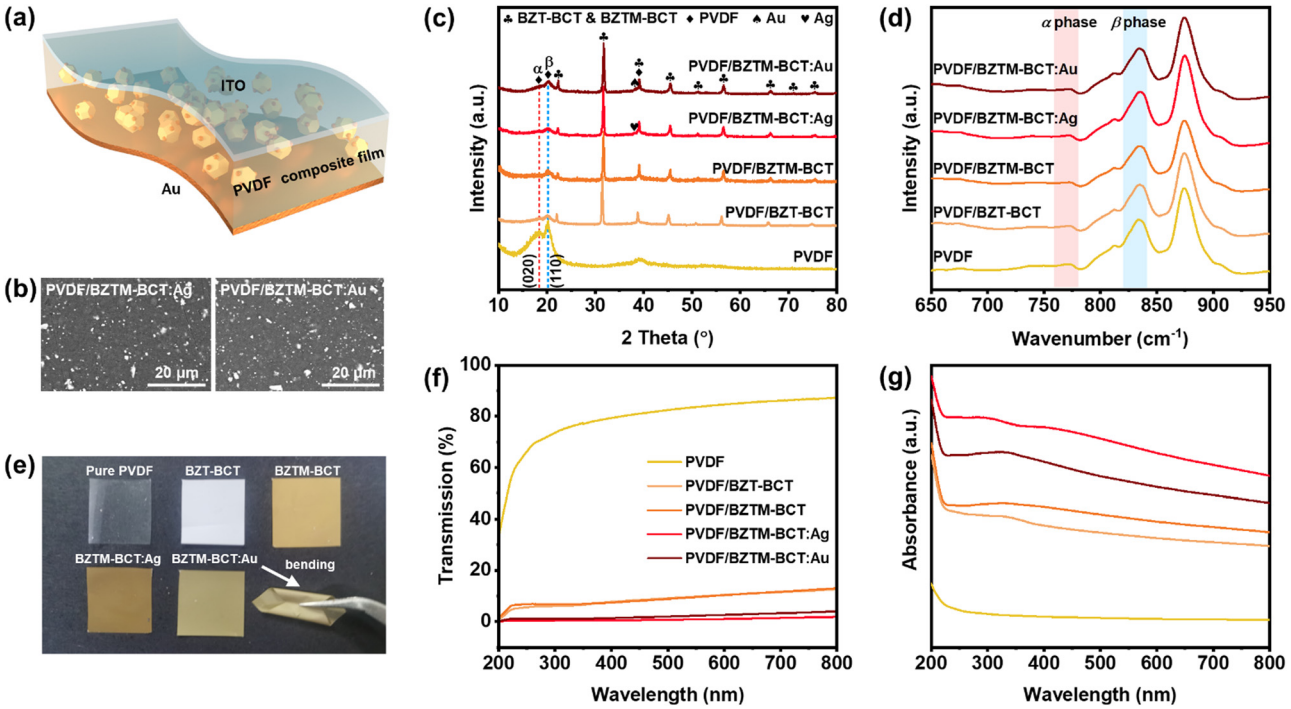

Fig. 2 Structure and physical characterizations of PVDF composite films. (a) Schematic of the PVDF composite films. (b) SEM images for PVDF/BZTM–BCT:Au and PVDF/BZTM–BCT:Ag films. The XRD patterns (c), FTIR spectra (d), photographs (e), transmission (f) and absorbance (g) of PVDF composite films.

indicating their excellent flexibility. The practical transmissions and absorbances were collected through testing UV-vis spectra (Fig. 2f and g); the results of which are consistent with the color variation of the composite films. The highest transmission but lowest absorption is observed for the pure PVDF film. On embedding the BZT–BCT and BZTM–BCT particles, the light is absorbed and scattered simultaneously by these particles. Thus, it is difficult for the light to fully pass through the composite films, resulting in largely decreasing transmission. Due to the similar content and distribution of BZT–BCT and BZTM–BCT in PVDF, the PVDF/BZT–BCT and PVDF/BZTM–BCT films show almost identical transmission. However, because the BZTM–BCT particles exhibit greater absorption than the BZT–BCT particles, the light is more absorbed but less scattered in the PVDF/BZTM–BCT than PVDF/BZT–BCT film. In addition, the scattering interface between PVDF and the ceramic particles may lead to a change in the refractive index of the film. Therefore, although the PVDF and BZT–BCT composites both exhibit almost negligible absorption in the visible light region, the PVDF/BZT–BCT composite film presents visible light absorption. After depositing Au and Ag NPs on the BZTM–BCT particles, the stronger absorption and greater scattering interface in the BZTM–BCT:Au/Ag particles cause the transmission/absorption to further decrease/increase.

Photovoltaic properties

The flexible PVDF composite film schematically demonstrated in Fig. 2a was further investigated for its photovoltaic properties. Different testing states and corresponding energy band structures are schematically described in Fig. 3a to explain the photovoltaic mechanism. The Mn-doped BZT–BCT is regarded as an n-type semiconductor due to the acceptor doping.[30] Because of the work function difference between the Au (5.1 eV) and ITO (4.8 eV) electrodes,[38,39] a built-in field E_{bi} forms in the flat films, pointing from ITO to Au electrodes. When the films are bent upward, the top surface is stretched and the bottom surface is compressed, resulting in an upward strain gradient and downward electric field E_{flexo}, *i.e.*, the flexoelectric effect. An additional downward polarization field (E_{ps}) appears upon further upward poling of the films, corresponding to the "bending + poling" samples. E_{flexo} and E_{ps} have the same direction with E_{bi}, which leads to the energy barrier height decreasing in the ITO side, but increasing in the Au side. This change is likely to promote carrier transport and improve the photocurrent.

Fig. 3b–d presents the time-dependent photocurrents (I_{ph}) at zero-bias under three states when illuminated with 405 nm light at 100 mW cm^{-2}. The corresponding photocurrents are summarized in Table S1 (ESI†). For all of the samples under any state, the dark currents are pretty small at only a few pA. Under light illumination and a flat state, the pure PVDF film exhibits almost negligible I_{ph} (about 0.07 nA). The I_{ph} slightly increases after introducing the BZT–BCT (0.12 nA) and BZTM–BCT (0.28 nA) particles. A higher I_{ph} for the PVDF/BZTM–BCT film compared to the PVDF/BZT–BCT film is reasonable due to its stronger photo absorption. Interestingly, depositing Ag and Au NPs on the BZTM–BCT particles causes a significant increase of the I_{ph} in the films, reaching up to 0.82 and 1.21 nA for the PVDF/BZTM–BCT:Ag and PVDF/BZTM–BCT:Au films, respectively. These values are 3 and 4.5 times higher than that of the PVDF/BZTM–BCT film, and one order of magnitude higher

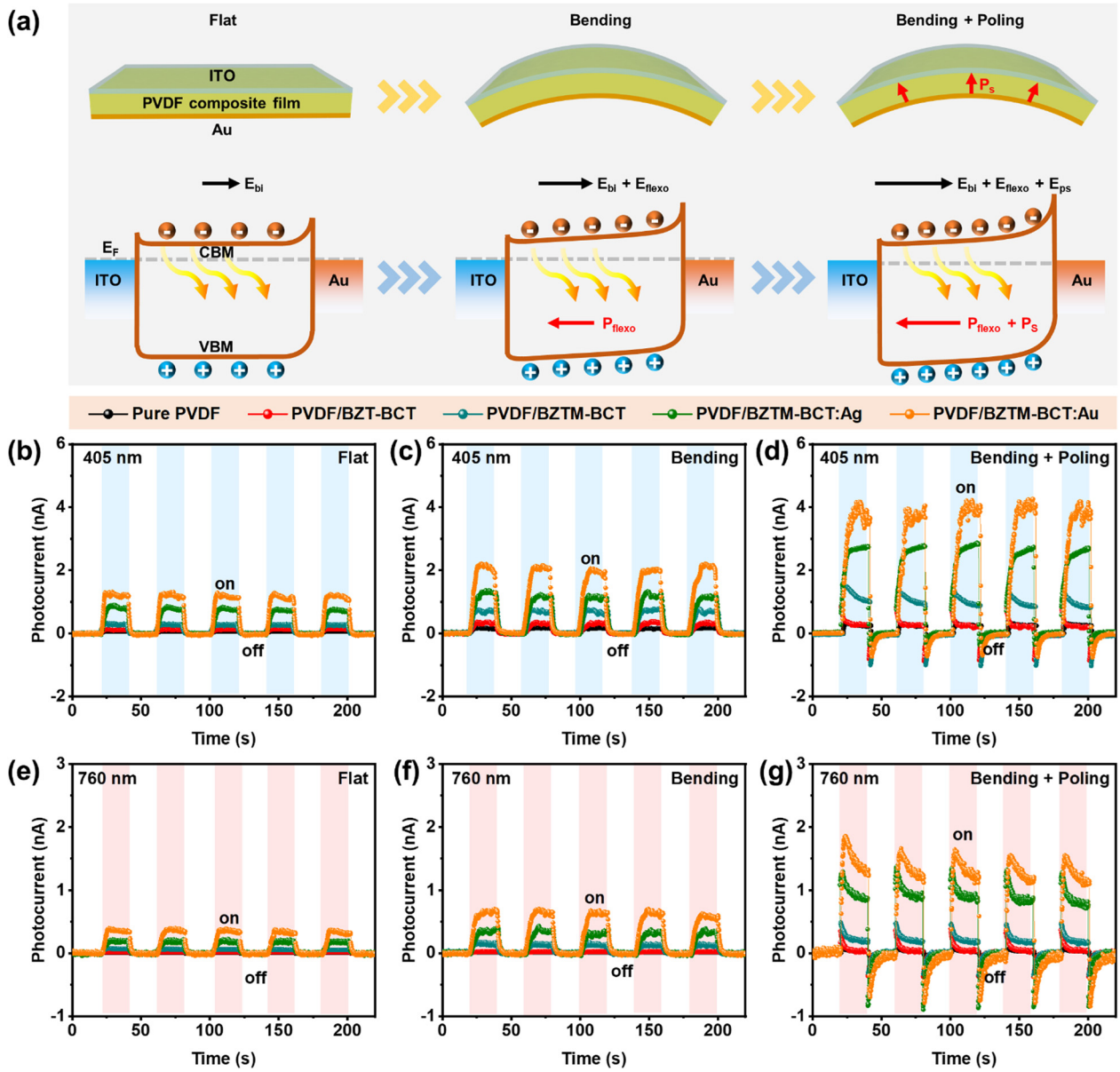

Fig. 3 Comparison of the photovoltaic properties of different PVDF composite films. (a) Different states of films, including flat, bending and bending after poling, as well as the corresponding energy band structures. E_{bi}, E_{flexo} and E_{ps} represent the electric field created by Schottky barriers, flexoelectric polarization and ferroelectric polarization, respectively. The photocurrent–time curves of the five composite films under 405 nm (b)–(d) and 760 nm (e)–(g) LED light irradiation, tested for the flat samples (b) and (e), bending samples (c) and (f) and bending samples after poling (d) and (g). The light intensity is fixed at 100 mW cm^{-2}.

than that of the pure PVDF film. This is mainly caused by the greater number of generated carriers, which will be discussed in detail in the following section.

The value for I_{ph} is further increased on account of the flexoelectric effect, which is induced by bending the films. For the PVDF/BZTM–BCT:Au film, I_{ph} reaches about 2.1 nA, which is 75% higher than that observed under a flat state. Furthermore, on poling the composite films and testing their I_{ph} in the bending state, the I_{ph} for all five films increases, while their difference becomes quite significant. For films with Au and Ag NPs, I_{ph} is obviously higher than the others. Specifically for the PVDF/BZTM–BCT:Au film, I_{ph} increases to about 4.0 nA, an enhancement of 86% compared to the pre-poling state. In addition, obvious and similar peak currents are observed in all composite films when the light is turned off, which is caused by the pyroelectric effect and explained in Fig. S5 (ESI†). Overall, in all of the films, I_{ph} of the flexible PVDF-based photovoltaic device increases by 57 times through coupling the composite film preparation, flexoelectric effect and ferroelectric polarization. More importantly, the photovoltaic responses of the composite films are extended to 760 nm (Fig. 3e–g). There are no I_{ph} for the pure PVDF film and PVDF/BZT–BCT film under the three states irradiated by 760 nm light. This is due to the narrow photo absorption range of the PVDF and

BZT–BCT composites. The photovoltaic response is generated after Mn doping BZT–BCT, and is substantially improved after depositing Ag or Au NPs on the BZTM–BCT particles. Comparatively, the PVDF/BZTM–BCT:Au film exhibits a maximum photocurrent of 1.3 nA under the "poling + bending" state. The I_{ph} changes under different states are also verified by measuring and plotting the photocurrent–voltage (I–V) curves (Fig. S6, ESI†). Whether the voltage is applied or not, the I_{ph} increases after bending and poling. Concurrently, the open circuit voltage (V_{oc}) slightly increases from about 0.2 V to over 0.3 V. The I_{ph}–t curves of the upward bending samples under downward poling are presented in Fig. S7 (ESI†). In this case, E_{ps} is in the opposite direction to E_{bi} and E_{flexo}, which weakens or even flips the downward electric field. Therefore, the photovoltaic currents almost disappear for the pure PVDF, PVDF/BZT–BCT and PVDF/BZTM–BCT films, while the PVDF/BZTM–BCT:Au and PVDF/BZTM–BCT:Ag films exhibit negative photovoltaic currents. In addition, when the light turns on/off, the pyroelectric peak current that occurs opposite to that in the upward poled samples is caused by the reverse dipole moment.

The I_{ph} adjustability of the poled PVDF/BZTM–BCT:Au composite film was studied. Firstly, the photocurrent is nonlinearly dependent on the bending extent. Under 405 nm light illumination, the I_{ph} increases when the distance between the two terminals decreases from 17 (flat state) to 13 mm (bending state). Meanwhile, a larger bending extent causes the effective irradiation area to significantly decrease. Thus, the I_{ph} is decreased (Fig. 4a), which is schematically depicted in Fig. S8 (ESI†). The film exhibits a photovoltaic response in the whole visible light range, and the magnitude is almost consistent with the absorption ability to light with the corresponding wavelength (Fig. 4b). Therefore, it is reasonably believed that the composite film exhibits a photoresponse even under the illumination of near-infrared light. By contrast, the I_{ph} of the pure PVDF film is very weak under all of the used lights (Fig. S9, ESI†).

Fig. 4c displays the changes in the temperature and I_{ph} of the PVDF/BZTM–BCT:Au film with different 405 nm light intensities under the "bending + poling" state. Unlike most reported ferroelectric materials with a linear dependence of I_{ph} on the light intensity, the I_{ph} of the composite film increases quasi-exponentially with increasing light intensities. This phenomenon can be analyzed by eqn (2):

$$I_{ph} = Sq\mu(n_{ph} + n_T)E \quad (2)$$

where S, q, μ and E are constants for specific materials at zero bias, representing the effective electrode area, the charge of an electron, carrier mobility and built-in electric field, respectively. n_{ph} and n_T are the generated electrons caused by photon and thermal excitations, respectively. According to the semiconductor theory, n_{ph} is linearly dependent on the light intensity P, while n_T nonlinearly depends on temperature T, given by eqn (3) and (4), respectively:

$$n_{ph} \propto G\alpha P \quad (3)$$

$$n_T \propto AT^{3/2}\exp\left(-\frac{\phi}{kT}\right) \quad (4)$$

where G, α, A and k are the Gaussian coefficient, photo absorption coefficient, parameter related to materials, and Boltzmann

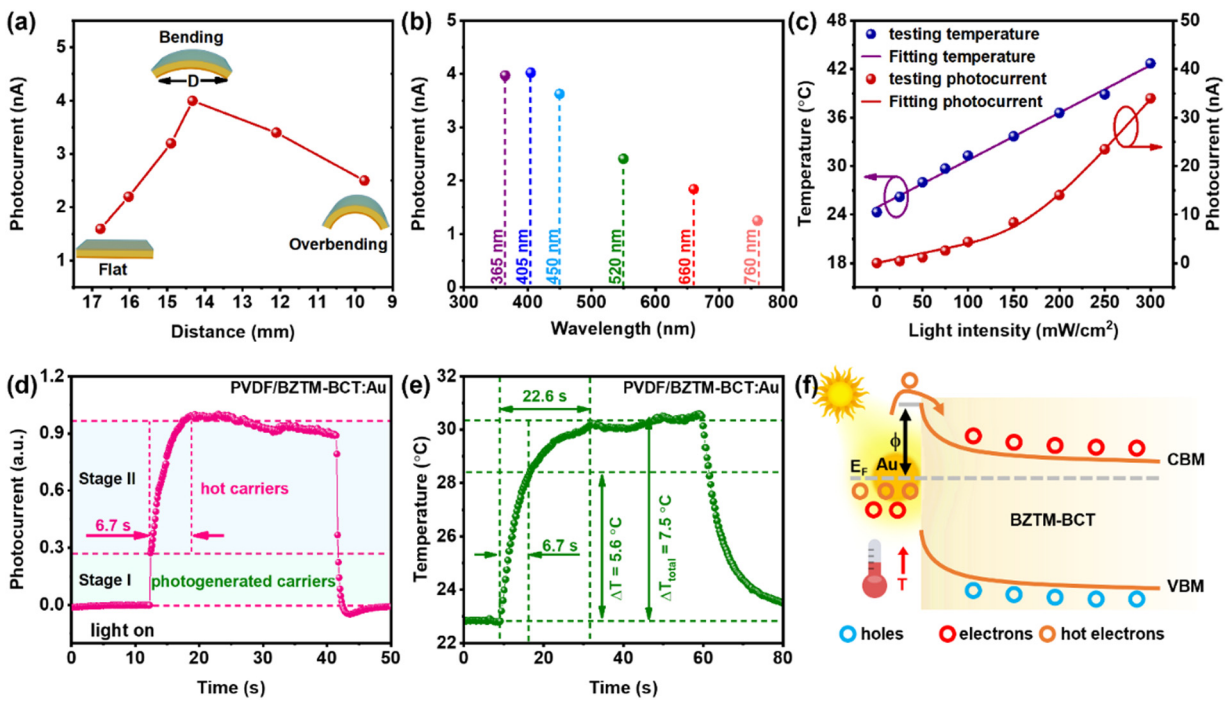

Fig. 4 Photocurrent and photoresponse mechanism analysis of the PVDF/BZTM–BCT:Au composite film with 405 nm LED light. Photocurrent dependence on the bending extent (a), light wavelength (b) and light intensity (c). (d) Photocurrent and (e) temperature change with time. (f) Energy band structure of the Au NPs-deposited BZTM–BCT particles.

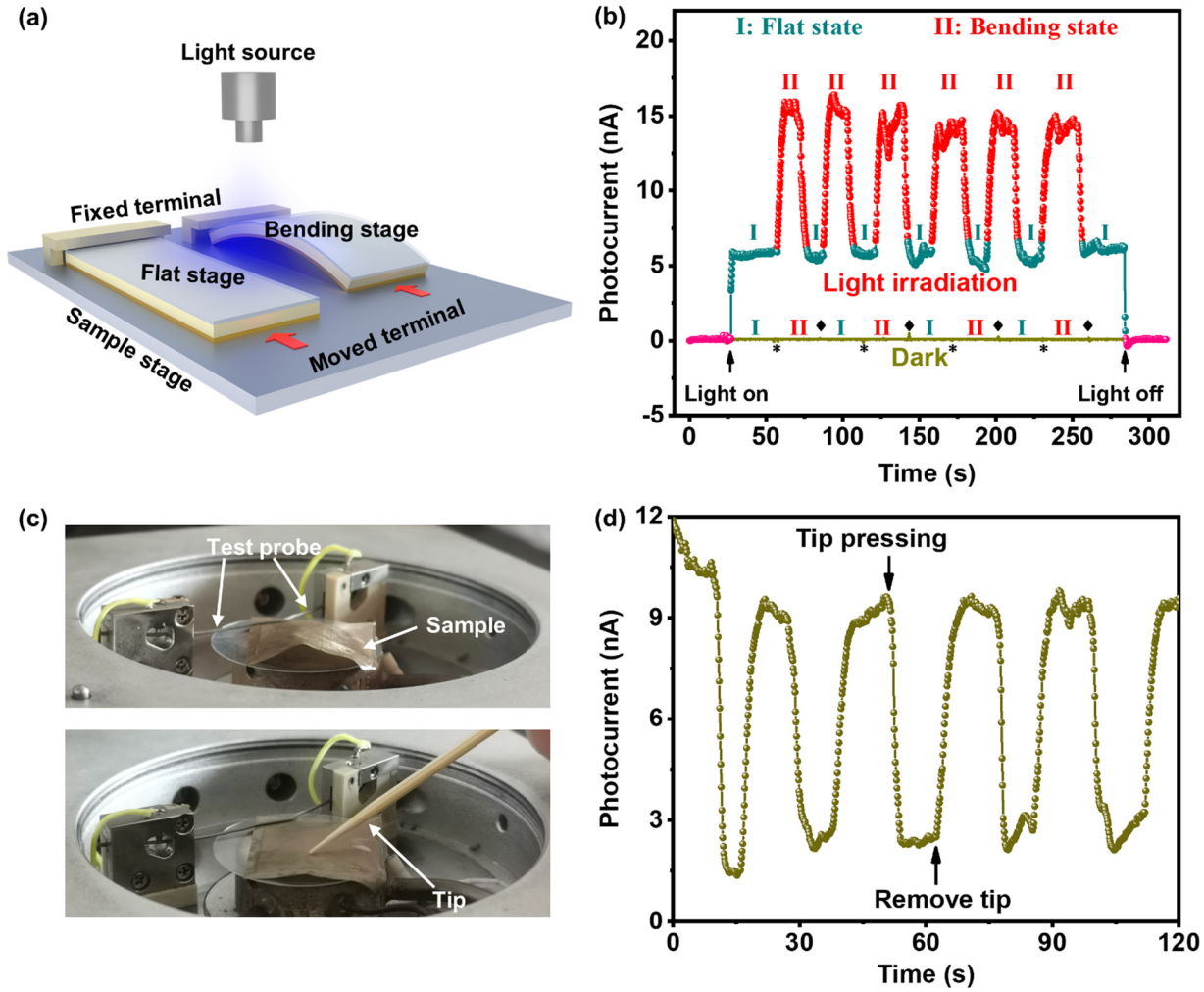

Fig. 5 The photocurrent changes with bending states. (a) Schematics of the flat and bending films. (b) Photocurrent evolution with the bending film under light irradiation and dark conditions. The symbols "*" and "♦" under dark condition mean that the film starts to bend and flatten, respectively. (c) Film before tip pressing and after removing tip. (d) Photocurrent corresponding to (c).

constant, respectively. They are all constants. ϕ is the Schottky barrier between the Au NPs and BZTM–BCT particles. Due to the linearly increasing film temperature with increasing light intensities (the T–P curve in Fig. 4c), the relationship between I_{ph} and P can be expressed by:

$$I_{ph} \propto G\alpha P + AP^{\frac{3}{2}} \exp\left(-\frac{\phi}{kP}\right) \quad (5)$$

It can be seen that the I_{ph}–P curve obtained from the above formula fits well with the tested values, which indicates that the photoelectric response is simultaneously contributed by the photo light energy and heat energy. This speculation is further confirmed by the time-dependent photocurrent and temperature. Fig. 4d presents the normalized I_{ph} of the PVDF/BZTM–BCT:Au composite film under 405 light of 100 mW cm^{-2}. It is obvious that the rising process is divided into two stages, including the rapidly increasing stage I and slowly increasing stage II. The photogenerated carriers are often separated and transported in a very short time, which is consistent with stage I. The time span in stage II is 6.7 s. During this time, the film temperature increases by 5.6 °C, which is 75% of the entire increase in film temperature (7.5 °C in 22.6 s), as shown in Fig. 4e. Therefore, it is reasonable to attribute stage II to thermal excitation. In this process, the hot carrier concentration slowly increases with increasing film temperature, resulting in the long rising time of I_{ph}. It can be found that the photocurrent in stage II accounts for about 73% of the whole photocurrent, indicating the significant role that the hot carriers played in the photovoltaic response of the composite film. Due to the open measurement environment with slightly unstable temperature, I_{ph} slightly fluctuates and decreases after stage II. The PVDF/BZTM–BCT:Ag film also displays similar double stages, while the other composite films only exhibit the rapidly increasing photocurrent (Fig. S10, ESI†). Concurrently, the PVDF/BZTM–BCT composite film shows an almost linear photocurrent-light intensity curve (Fig. S11, ESI†). These phenomena indicate the strong relationship between the metal NPs and hot carrier excitation. This can be explained by the energy band structure of the BZTM–BCT:Au heterostructure (Fig. 4f). Under light illumination, film temperature increases due to the

photothermal effect, accompanied by the temperature increase of Au NPs. Therefore, a lot of electrons are thermally excited and jump into the conductive band of the BZTM–BCT sample with the help of the Au/BZTM–BCT Schottky junction. In terms of this perspective, the relatively small I_{ph} of the PVDF/BZTM–BCT:Ag composite film may be due to the lower work function ($\sim$4.5 eV) of Ag, which results in a far lower Schottky barrier height and subsequent easier combination of electron–hole pairs in Ag/BZTM–BCT than the Au/BZTM–BCT interface. The hot carrier mechanism here is also used to explain the difference of the peak current under 405 nm and 760 nm light. As shown in Fig. S12 (ESI†), the photocurrents of the PVDF/BZTM–BCT:Ag and PVDF/BZTM–BCT:Au composite films consist of the pyroelectric current (I_{py}) and photovoltaic current (I_{pv}) generated by photon and thermal excitations, respectively. I_{py} increases at the moment when the light turns on and then gradually decreases, while I_{pv} gradually increases and then remains stable. Under 405 nm light, the increasing rate of I_{pv} is faster than the decreasing rate of I_{py} before they reach a stable state. Therefore, no peak current is observed in the PVDF/BZTM–BCT:Au and PVDF/BZTM–BCT:Ag films when the light is on. However, under 760 nm light, the rising rate of I_{pv} is faster at first and then slower than the decreasing rate of I_{py}, resulting in the occurrence of the peak current after a short period of light irradiation. When the PVDF/BZTM–BCT:Au composite film changes from flat to bending stages (Fig. 5a), the corresponding photocurrent dynamically evolves under 405 nm light illumination of 200 mW cm^{-2} (Fig. 5b). It can be seen that the photocurrent continuously increases from about 5 nA to 15 nA as the distance between the two terminals decreases from 17 to 13 mm. No obvious leap is observed. This phenomenon indicates the sensitivity of this flexible photoelectric sensor in response to film bending. In addition, there is almost no current response when bending the film under dark condition. This means that the piezoelectric response of the composite film is pretty weak. Thus, under the bending state, the contribution of the piezoelectric potential to the photocurrent can be excluded. Moreover, the versatility of this flexible photoelectric sensor is realized. It can sense not only light, but also the change of the things contacted with it, including movement and deformation. More precisely, the detection must be operated under light illumination, where light acts as a switch to control the signal generation. Here, we simulate a scene of tip movement by poking the film with a toothpick (Video S1, ESI†). Because the film is naturally curved (upper image in Fig. 5c), it initially presents a high photocurrent of about 9 nA under light illumination. When the film is pressed by a toothpick tip (Fig. 5c), the film becomes flat and the photocurrent rapidly decreases to about 3 nA (Fig. 5d). The photocurrent recovers its original value after removing the tip. These results highlight that the composite film-based photoelectric sensors is versatile and can be applied to detect photons, and the movement and deformation of contacted things.

Conclusions

In summary, the versatile flexible photoelectric sensors are designed by embedding the Au and Ag NPs-loaded BZTM–BCT particles into the PVDF film. The metal NPs/BZTM–BCT heterojunction is well constructed and presents excellent photo absorption in the whole visible light range. The composite particles not only make the polar β content of the film reach 93%, but also significantly enhance the photovoltaic response of PVDF from 405 nm to 760 nm. Through coupling of the composite film preparation, film bending and poling, the PVDF/BZTM–BCT:Au composite film presents an optical photocurrent that is 57 times higher than that of the pure PVDF film under 405 nm light of 100 mW cm^{-2}. The hot carriers from Au NPs to BZTM–BCT contribute 73% of the photocurrent. Furthermore, due to its photocurrent dependence on the bending extent, the flexible photoelectric sensor can simultaneously sense photons and the movement and deformation of things. These results indicate the versatile application of the composite film.

Author contributions

L. W. and Z. Y. proposed the experimental scheme. L. W. carried out the experiment. All authors analyzed and discussed the results. L. W., M. A. B. and Z. Y. edited the manuscript. All authors have given approval to the final version of the manuscript.

Data availability

The data supporting this article have been included as part of the ESI.†

Conflicts of interest

There are no conflicts to declare.

Acknowledgements

This work was financially supported by the National Natural Science Foundation of China (Grant No. 52372130, 52202152 and 52250410356), the Natural Science Foundation of Shanghai (Grant No. 22ZR1471200), the Future Partner Special Project of the Chinese Academy of Sciences (Grant No. 030GJHZ2023076FN), the Frontier Science Key Project of the Chinese Academy of Sciences (Grant No. QYZDB-SSW-JSC027) and the Instrument Developing Project of Chinese Academy of Sciences (Grant No. ZDKYYQ20180004).

Notes and references

1 Y. Tang, P. Jin, Y. Wang, D. Li, Y. Chen, P. Ran, W. Fan, K. Liang, H. Ren, X. Xu, R. Wang, Y. M. Yang and B. Zhu, *Nat. Commun.*, 2023, **14**, 4961.
2 P. Rong, S. Gao, S. Ren, H. Lu, J. Yan, L. Li, M. Zhang, Y. Han, S. Jiao and J. Wang, *Adv. Funct. Mater.*, 2023, **33**, 2300159.
3 J. Lee, H. J. Kim, Y. J. Ko, J. Y. Baek, G. Shin, J. G. Jeon, J. H. Lee, J. H. Kim, J. H. Jung and T. J. Kang, *Nano Energy*, 2022, **97**, 107178.

4 S. Cai, X. Xu, W. Yang, J. Chen and X. Fang, *Adv. Mater.*, 2019, **31**, e1808138.
5 X. He, C. Chen, C. Li, H. Zeng and Z. Yi, *Adv. Funct. Mater.*, 2019, **29**, 1900918.
6 T. Choi, S. Lee, Y. J. Choi, V. Kiryukhin and S.-W. Cheong, *Science*, 2009, **324**, 63–66.
7 S. Y. Yang, J. Seidel, S. J. Byrnes, P. Shafer, C. H. Yang, M. D. Rossell, P. Yu, Y. H. Chu, J. F. Scott, J. W. AgerIII, L. W. Martin and R. Ramesh, *Nat. Nanotechnol.*, 2010, **5**, 143–147.
8 H. Liu, T. Zhao, W. Jiang, R. Jia, D. Niu, G. Qiu, L. Fan, X. Li, W. Liu, B. Chen, Y. Shi, L. Yin and B. Lu, *Adv. Funct. Mater.*, 2015, **25**, 7071–7079.
9 T. Zhao, W. Jiang, H. Liu, D. Niu, X. Li, W. Liu, X. Li, B. Chen, Y. Shi, L. Yin and B. Lu, *Nanoscale*, 2016, **8**, 8111–8117.
10 D. Zabek, J. Taylor, E. L. Boulbar and C. R. Bowen, *Adv. Energy Mater.*, 2015, **5**, 1401891.
11 C.-M. Wu, M.-H. Chou, T. F. Chala, Y. Shimamura and R.-I. Murakami, *Compos. Sci. Technol.*, 2019, **178**, 26–32.
12 M. N. Islam, R. H. Rupom, P. R. Adhikari, Z. Demchuk, I. Popov, A. P. Sokolov, H. F. Wu, R. C. Advincula, N. Dahotre, Y. Jiang and W. Choi, *Adv. Funct. Mater.*, 2023, **33**, 2302946.
13 Z. Zhou, Q. Zhang, Z. Zhang, H. Kuang, X. Du and H. Yang, *Chem. Eng. J.*, 2022, **442**, 136241.
14 S. Nadupalli, J. Kreisel and T. Granzow, *Sci. Adv.*, 2019, **5**, eaau9199.
15 M.-M. Yang, D. J. Kim and M. Alexe, *Science*, 2018, **360**, 904–907.
16 J. H. Haeni, P. Irvin, W. Chang, R. Uecker, P. Reiche, Y. L. Li, S. Choudhury, W. Tian, M. E. Hawley Craigo, A. K. Tagantsev, X. Q. Pan, S. K. Streiffer, L. Q. Chen, S. W. Kirchoefer, J. Levy and D. G. Schlom, *Nature*, 2004, **430**, 758–761.
17 Y. Xia, Y. Ji, Y. Liu, L. Wu and Y. Yang, *ACS Appl. Mater. Interfaces*, 2022, **14**, 36763–36770.
18 B. Zhang, C. Guo, X. Cao, X. Yuan, X. Li, H. Huang, S. Dong, Z. L. Wang and K. Ren, *Nano Energy*, 2022, **104**, 107897.
19 X. Liu, F. Zhang, P. Long, T. Lu, H. Zeng, Y. Liu, R. L. Withers, Y. Li and Z. Yi, *Adv. Mater.*, 2018, **30**, 1801619.
20 A. Biancoli, C. M. Fancher, J. L. Jones and D. Damjanovic, *Nat. Mater.*, 2015, **14**, 224–229.
21 A. Abdollahi, N. Domingo, I. Arias and G. Catalan, *Nat. Commun.*, 2019, **10**, 1266.
22 L. Shu, S. Ke, L. Fei, W. Huang, Z. Wang, J. Gong, X. Jiang, L. Wang, F. Li, S. Lei, Z. Rao, Y. Zhou, R.-K. Zheng, X. Yao, Y. Wang, M. Stengel and G. Catalan, *Nat. Mater.*, 2020, **19**, 605.
23 Q. Huang, Z. Fan, J. Rao, T. Yang, X. Zhang, D. Chen, M. Qin, M. Zeng, X. Lu, G. Zhou, X. Gao and J. M. Liu, *Adv. Electron. Mater.*, 2021, **8**, 2100612.
24 Y.-g Kim, H. Kim, G.-J. Lee, H.-U. Lee, S. G. Lee, C. Baek, M.-K. Lee, J.-J. Park, Q. Wang, S. B. Cho, C. K. Jeong and K.-I. Park, *Nano Energy*, 2021, **89**, 106469.
25 R. Guo, L. You, W. Lin, A. Abdelsamie, X. Shu, G. Zhou, S. Chen, L. Liu, X. Yan, J. Wang and J. Chen, *Nat. Commun.*, 2020, **11**, 2571.
26 H. You, S. Li, Y. Fan, X. Guo, Z. Lin, R. Ding, X. Cheng, H. Zhang, T. W. B. Lo, J. Hao, Y. Zhu, H. Y. Tam, D. Lei, C. H. Lam and H. Huang, *Nat. Commun.*, 2022, **13**, 6144.
27 Y. Zhu, B. Wang, C. Deng, Y. Wang and X. Wang, *Nano Energy*, 2021, **83**, 105801.
28 H. Liu, R. Zhu, N. Shi, L. Zhang, S. Li and J. Zhang, *ACS Appl. Mater. Interfaces*, 2022, **14**, 55548–55558.
29 R. Su, D. Zhang, M. Wu, F.-T. Li, Y. Liu, Z. Wang, C. Xu, X. Lou, Q. Yu and Y. Yang, *J. Alloys Compd.*, 2019, **785**, 584–589.
30 L. Wang, F. Zhang, C. Chen, X. He, M. A. Boda, K. Yao and Z. Yi, *Nano Energy*, 2024, **119**, 109081.
31 H. Li, H. Wang, X. Li, J. Huang, X. Li, S. K. Boong, H. K. Lee, J. Han and R. Guo, *Nano Energy*, 2022, **100**, 107527.
32 M. Yan, S. Liu, Y. Liu, Z. Xiao, X. Yuan, D. Zhai, K. Zhou, Q. Wang, D. Zhang, C. Bowen and Y. Zhang, *ACS Appl. Mater. Interfaces*, 2022, **14**, 53261–53273.
33 P. Martins, A. C. Lopes and S. Lanceros-Mendez, *Prog. Polym. Sci.*, 2014, **39**, 683–706.
34 L. Ruan, X. Yao, Y. Chang, L. Zhou, G. Qin and X. Zhang, *Polymers*, 2018, **10**, 228.
35 H. Z. Li, W. Z. Li, Y. J. Yang, H. L. Tai, X. S. Du, R. Y. Gao and S. Y. Li, *Ceram. Int.*, 2018, **44**, 19254–19261.
36 Y. Huan, X. Zhang, J. Song, Y. Zhao, T. Wei, G. Zhang and X. Wang, *Nano Energy*, 2018, **50**, 62–69.
37 C. Baek, J. H. Yun, J. E. Wang, C. K. Jeong, K. J. Lee, K. I. Park and D. K. Kim, *Nanoscale*, 2016, **8**, 17632–17638.
38 H. Zhou, Q. Chen, G. Li, S. Luo, T.-B. Song, H.-S. Duan, Z. Hong, J. You, Y. Liu and Y. Yang, *Science*, 2014, **345**, 542–546.
39 R. Zhao, N. Ma, K. Song and Y. Yang, *Adv. Funct. Mater.*, 2019, **30**, 1906232.